Supporting Information for

Post-plasma catalytic model for NO production: Revealing the underlying mechanisms to improve the process efficiency

Hamid Ahmadi Eshtehardi[a,b,*], Kevin Van ‘t Veer[a,c], François Reniers[c], Marie-Paule Delplancke[b], Annemie Bogaerts[a,*]

[a] Research group PLASMANT, University of Antwerp, Department of Chemistry, Universiteitplein 1, BE-2610 Wilrijk-Antwerp, Belgium

[b] Research group 4MAT, Université Liberé De Bruxelles, 50 Rossvelt Av., CP 165/63, 1050 Brussels, Belgium

[c] Chemistry of Surfaces, Interfaces and Nanomaterials (ChemSIN), Faculty of Science, Université Libre De Bruxelles, Avenue F.D. Roosevelt 50, 1050 Brussels, Belgium

*Corresponding authors

Prof. Dr. Annemie Bogaerts
Address: Research group PLASMANT, University of Antwerp, Department of Chemistry, B 2.09, Universiteitplein 1, BE-2610 Wilrijk-Antwerp, Belgium.
Tel.: +32 (0)3 265 2377
E-mail: annemie.bogaerts@uantwerpen.be

Hamid Ahmadi Eshtehardi:
Address: Research group PLASMANT, University of Antwerp, Department of Chemistry, B 2.29, Universiteitplein 1, BE-2610 Wilrijk-Antwerp, Belgium.
Tel.: +32 (0)3 265 9263
E-mail: hamid.ahmadieshtehardi@uantwerpen.be

SI includes 29 pages, 8 figures and 2 tables.

SI.1. Technical details and empirical correlations for the calculation of the physical properties in the model

As mentioned in section 2.4 of the main paper, several physical parameters are used in our model for which we used empirical correlations that according to literature were successful in modelling fixed bed catalytic reactors. In this section we present the technical information for calculation of these physical parameters.

SI.1.1. Gas-to-solid mass and heat transfer coefficient

The gas-to-solid mass transfer coefficient of species i in the gas phase, $k_{g,i}$ $(\mathrm{m}^3(\mathrm{m}^2\ \mathrm{s})^{-1})$, can be calculated using the following correlation [1], [2]

$$k_{g,i} = j_{D,i} Re Sc_i^{1/3} \frac{D_i}{d_p} \tag{S1}$$

$$j_{D,i} = \frac{Sh}{Re Sc_i^{1/3}} \tag{S2}$$

In eq. S2, $j_{D,i}$ is the Chilton-Colburn factor for mass transfer, Sh, and Sc_i are the Sherwood and Schmidt dimensionless numbers, respectively, which are given by [1], [3], [4]:

$$Sc_i = \frac{\mu_g}{\rho_g D_i}; \text{for } 0.6 < Sc < 7000, \text{and } 0.25 < \varepsilon_b < 0.96 \tag{S3}$$

$$Sh = 2 + 1.1 Sc^{1/3} Re^{0.6} \tag{S4}$$

Where μ_g is the gas dynamic viscosity (kg $\mathrm{m}^{-1}\mathrm{s}^{-1}$).

Similarly, in order to determine the heat transfer coefficient, h_f(W $(\mathrm{m}^2\ \mathrm{K})^{-1}$), the following relation can be used [2], [5]:

$$h_f = j_H \frac{C_{pg} G_s}{Pr^{2/3}} \tag{S5}$$

Where G_s is the mass velocity of the gas phase (kg $(\mathrm{m}^2\ \mathrm{s})^{-1}$), and j_H is Chilton-Colburn factor for heat transfer and is given by [2]:

$$j_H = \frac{Nu}{Re Pr^{1/3}} \tag{S6}$$

Where Nu is the Nusselt dimensionless number. The following relation is recommended for determining the Nu number in packed beds [3], [4]:

$$Nu = 2 + 1.1 Pr^{1/3} Re^{0.6} \tag{S7}$$

SI.1.2. Axial dispersion coefficient

The axial dispersion coefficient, D_z $(\mathrm{m}^2\mathrm{s}^{-1})$, is a measure of the degree of spread of an inert trace material along a tubular vessel longitudinal direction. It is a coefficient that can characterize the degree of back-mixing and quantify the deviation from ideal plug flow behavior and it is given as [6]:

$$D_z = 0.73 D_m + \frac{0.5 u_s d_p}{1 + 9.49\, D_m / u_s d_p} \tag{S8}$$

Where D_m is the average molecular diffusivity $(\mathrm{m}^2\mathrm{s}^{-1})$ and u_s is the superficial gas velocity (m s^{-1}).

The average molecular diffusivity, D_m, can be calculated as:

$$D_m = \frac{RT}{P}\sum C_i D_i \tag{S9}$$

Where C_i is the concentration of species i in the gas phase ($\mathrm{mol\,m^{-3}}$), R is the gas universal constant ($\mathrm{J(K\,mol)^{-1}}$), P is the total pressure of the system (Pa), and D_i is the effective diffusion coefficient ($\mathrm{m^2\,s^{-1}}$) of species i in the gas phase and is calculated as follows [7]:

$$D_i = \frac{1}{\left({}^{\tau_{cat}}/_{\varepsilon_b}\right)\left(\frac{1}{D_{Amix}} + \frac{1}{D_{Kn,i}}\right)} \tag{S10}$$

Where $\mathrm{\varepsilon_b}$ is the catalyst bed porosity, which is defined as:

$$\varepsilon_b = 1 - \frac{V_p}{V_t} \tag{S11}$$

Where V_p and V_t are the total volume of catalyst particles and catalyst bed (m^3), respectively. τ_{cat} is the catalyst tortuosity factor, which is a helpful measure of the effects of pore structure on diffusion in catalyst particles [8], and can be calculated as follows [9]:

$$\tau_{cat} = \sqrt{\frac{\varepsilon_b}{(1-(1-\varepsilon_b)^{1/3})}} \tag{S12}$$

In eq. S15, D_{Amix} ($\mathrm{m^2\,s^{-1}}$) is the molecular diffusion coefficient of species A in the gas mixture, calculated by Blanc's law [10]:

$$\frac{1}{D_{Amix}} = \sum_i x_a \frac{1}{D_{AB}} \tag{S13}$$

Where D_{AB} ($\mathrm{m^2\,s^{-1}}$) is the binary molecular diffusion coefficient of species A into each of the other species (B) that are present in the gas phase, and x_a is the mole fraction of species A in the gas phase. D_{AB} is given using the following equation [11]:

$$D_{AB} = \frac{1.00 \times 10^{-3} T^{1.75} (1/M_A + 1/M_B)^{1/2}}{p[(\Sigma_A v_i)^{1/3} + (\Sigma_B v_i)^{1/3}]^2} \times 10^{-4} \tag{S14}$$

Where M_A and M_B are the molecular weights ($\mathrm{g\,mol^{-1}}$) of species A and B, respectively, p is the pressure in atm and T is the temperature in K. $\Sigma_A v_i$ and $\Sigma_B v_i$ are the sum of special atomic diffusion volumes of the atoms that are forming species A and B, respectively, and their values for simple gas molecules and some atoms are presented in table S.1.

Table S1. Special atomic and molecular diffusion volumes [11], [12].

Atomic and structural diffusion volume increments			
C	15.9	F	14.7
H	2.31	Cl	21.0
O	6.11	Br	21.9
N	4.54	I	29.8
Aromatic ring	-18.3	S	22.9
Heterocyclic ring	-18.3		
Diffusion volumes of simple molecules			
He	2.67	CO	18.0
Ne	5.98	CO_2	26.9
Ar	16.2	N_2O	35.9
Kr	24.5	NH_3	20.7

Xe	32.7	H_2O	13.1
H_2	6.12	SF_6	71.3
D_2	6.84	Cl_2	38.4
N_2	18.5	Br_2	69.0
O_2	16.3	SO_2	41.8
Air	19.7		

Finally, in eq.S15, $D_{Kn,i}$ is the Knudsen diffusion coefficient ($\mathrm{m^2 s^{-1}}$) of species i in the gas phase, which can be calculated as follows [7]:

$$D_{Kn,i} = \frac{d_{pore}}{3}\sqrt{\frac{8RT}{\pi M_i}} \tag{S15}$$

Where M_i is the molecular weight of species i ($\mathrm{g\ mol^{-1}}$), and d_{pore} is the diameter of the catalyst pores (m). The experimental value for this parameter (i.e., d_{pore}) was not given by Ma et al.[13]. Fang et al. [14], studied the effect of platinum on the sintering morphology of YSZ ceramics, and the reported value for the pore diameter was 10.4×10^{-9} m. As this was the same catalyst combination as used by Ma et al.[13], we assumed this value in our model.

SI.1.3. Effective thermal conductivity

The effective thermal conductivity, λ_z^f, is given by the following relation [15]:

$$\frac{\lambda_z^f}{\lambda_g} = \frac{\lambda_z^\circ}{\lambda_g} + 0.75PrRe \tag{S16}$$

and

$$\frac{\lambda_z^\circ}{\lambda_g} = \varepsilon_b + \frac{1-\varepsilon_b}{0.139\varepsilon_b - 0.0339 + \dfrac{\left(\frac{2}{3}\right)\lambda_g}{\lambda_s}} \tag{S17}$$

Where λ_g , λ_z^f , λ_z°, and λ_s are the average gas, effective, axial, and solid thermal conductivities ($\mathrm{W\ (m\ K)^{-1}}$), respectively. Pr and Re are the Prandtl and Reynolds dimensionless numbers, respectively, that are given as:

$$Re = \frac{\rho_g u_s d_p}{\mu_g};\ \ 0.1 < Re < 1500 \tag{S18}$$

$$Pr = \frac{C_{pg}\mu_g}{\lambda_g} \tag{S19}$$

Where ρ_g is the density of the gas phase ($\mathrm{kg\ m^{-3}}$), u_s is the gas phase superficial velocity ($\mathrm{m\ s^{-1}}$), d_p is the diameter of the catalyst particles (m), μ_g is the gas dynamic viscosity ($\mathrm{kg\ (m\ s)^{-1}}$), and C_{pg} is the heat capacity of the gas phase ($\mathrm{J\ (kg\ K)^{-1}}$).

SI.1.4. Catalyst effectiveness factor

When the reactants must diffuse inside the catalyst particles in order to react, the concentration at the pore mouth must be higher than inside the pore. Consequently, the entire catalytic surface is not accessible to the same concentration, and as a result the reaction rate through the catalyst particles will vary. To account for these variations, a parameter known as the catalyst effectiveness factor, η_j, is introduced, which is the ratio of overall reaction rate in the catalyst particle to the reaction rate at the external surface of the catalyst particle. In simple words, the effectiveness factor is a measure for how far the reactant diffuses into the catalyst particles before reacting [16]. The Thiele modulus (ϕ) describes the relationship between diffusion and reaction rates in porous catalyst particles with no mass transfer limitations and is generally used to measure the effectiveness factor of catalyst particles [17]. For a first order reaction in a spherical catalyst particle, the Thiele modulus and the effectiveness factor are related to each other as [16], [18]:

$$\eta\phi_1^2 = 3(\phi_1 coth\phi_1 - 1), \qquad \phi_1 \propto R \tag{S20}$$

Where ϕ_1 is the Thiele modulus for a first order reaction and R is the radius of the catalyst particle. As the particle diameter becomes very small, the Thiele modulus decreases, so that the effectiveness factor approaches 1 and the reaction is surface reaction limited. On the other hand, when the Thiele modulus is large (e.g., ~ 30), the effectiveness factor is small (e.g., ~ 0.1), and the reaction is diffusion limited within the particle. Consequently, in this case, factors influencing the rate of external mass transport such as fluid velocity will have a negligible effect on the overall reaction rate. The catalyst structure used in the system under study is a network of percolated particles of the order of micron [13]. Therefore, we can assume that the diameters of the catalyst particles are small enough (i.e., smaller than 0.1 mm), so that the Thiele modulus is lower than 1, and thus intra-porous mass and energy transport limitations are neglected (i.e., each point on the interior of the catalyst particle surface is accessible for each species to react); therefore, the effectiveness factor, η_j, is assumed to be unity in our model, for all the reactions.

SI.2. Calculation of adsorption, desorption and surface reaction rate coefficients

The rate coefficients for adsorption, desorption and surface reactions on Pt are defined based on transition state (TS) theory [19].

$$k = A\, exp\left(-\frac{E_a}{k_B T}\right) \tag{S21}$$

$$A = \frac{k_B T}{h}\, exp\left(\frac{\Delta S^{\circ}_{TS}}{k_B}\right) \tag{S22}$$

Where k_B is the Boltzmann constant, T is the absolute temperature, h is the Planck constant, ΔS°_{TS} is the standard entropy difference between the transition state and the initial state, and E_a is the activation energy of the reaction, as listed in table 2 in the main paper. The entropy of gas molecules from the NIST-JANAF thermochemical database is used for adsorption reactions [20]. The entropies of the transition states are assumed to be equal to the summation of the corresponding atomic adsorbate entropies, since the diatomic transition state largely lost its molecular identity and resembles the dissociated atoms [21]. The entropies of the atomic adsorbates over Pt(211) are taken from Ma et al. and Bajpai et al [22], [23]. The surface reactions are assumed to be entropy conservative and thus, $A = \frac{k_B T}{h}$.

The normalized density of each vibrationally excited state is estimated using the Treanor equation [24], [25]. The first ten vibrationally excited states are included because the higher excited levels have a lower population [13]. N_2 and O_2 are assumed to have the same vibrational temperature. Ma et al. estimated the vibrational temperature to be 10000 K in the plasma, based on [26], and they selected $T_v = 6000$ K as representative for the vibrational temperature drop expected during the post-plasma gas flow to the catalyst bed [13]. Therefore, $T_v = 6000$ K is also used in our model. The Treanor vibrational distribution function used in our model is expressed by eq. (S3) [24] and is presented in Fig, S.1 for both N_2 and O_2 molecules.

$$p_v(v, T_v, T_g) = \frac{exp\left(-\frac{\hbar\omega v}{T_v} + \frac{\hbar x_e \omega v^2}{T_g}\right)}{\sum_{v=0}^{10} exp\left(-\frac{\hbar\omega v}{T_v} + \frac{\hbar x_e \omega v^2}{T_g}\right)} \tag{S23}$$

Where $\hbar$ is the reduced Planck's constant, ω is the vibrational frequency, and x_e is the anharmonicity coefficient. ω of N_2 and O_2 are 2358.57 and 1580.16 cm^{-1}, respectively, while $x_e\omega$ are 14.324 and 11.951 cm^{-1}, respectively [27].

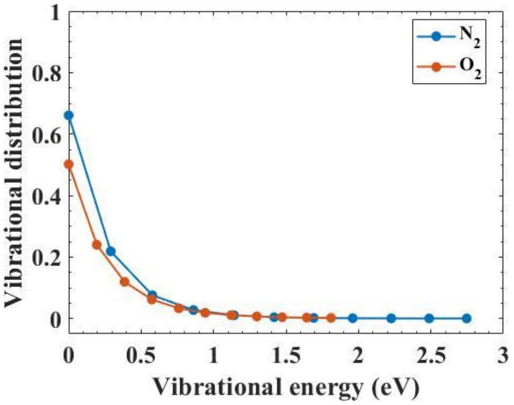

Figure S1. Treanor vibrational distribution function of N_2 and O_2 at $T_v = 6000\,K$ and $T_g = 873\,K$.

Vibrational excitation of N_2 and O_2 molecules reduces the activation energy barriers of the reactions involving these two species [25], [28]. Therefore, the rate constant of each vibrational state, v, of the Zeldovich and dissociative adsorption of N_2 and O_2 on Pt are written as:

$$k_v = A \exp\left(-\frac{E_a - \alpha E_v}{k_B T}\right) \tag{S24}$$

Where A is the pre-exponential factor as defined before, E_a is the activation energy of the ground vibrational state, E_v is the vibrational energy, α is the efficiency of vibrational excitation energy in overcoming the activation energy barrier. It is estimated with the Fridman-Macheret α-model, $\alpha = \frac{E_a^{(f)}}{E_a^{(f)} + E_a^{(b)}}$, where $E_a^{(f)}$ and $E_a^{(b)}$ are the activation barriers for the forward and backward reactions, respectively [25]. If $E_a - \alpha E_v \leq 0$ then $k_v = A$.

The overall rate coefficient for the dissociative adsorption of N_2 and O_2 is calculated as the summation of the rates at different vibrationally excited states times the population of the corresponding state (as determined from the vibrational distribution function) as follows:

$$k_{ads} = \sum_{v=0}^{10} p_v k_v \tag{S25}$$

SI.3. Dimensionless equations

By considering $\tau = \frac{t}{t_{res}}$ and $\zeta = \frac{z}{L}$, where t_{res} is the residence time and L is the characteristic length of the catalyst bed, and multiplying equations 1 to 4 by $\frac{t_{res}L^2}{t_{res}L^2}$, their dimensionless form against time and length can be derived as follows:

Mass and energy balance in the gas phase:

$$\frac{\partial C_i}{\partial \tau} + \frac{u_s t_{res}}{L\varepsilon_b}\frac{\partial C_i}{\partial \zeta} + \frac{t_{res}}{\varepsilon_b} k_{g,i} a_v \left(C_i - C_{i,s}\right) = \frac{t_{res} D_z}{L^2}\frac{\partial^2 C_i}{\partial \zeta^2} + \frac{t_{res}}{\varepsilon_b} r_i^{gas} \tag{S26}$$

$$\frac{\partial T}{\partial \tau} + \frac{u_s t_{res}}{L}\frac{\partial T}{\partial \zeta} = \frac{h_f a_v t_{res}}{\varepsilon_b \rho_g C_{pg}}(T - T_s) + \frac{\lambda_z^f t_{res}}{L^2 \varepsilon_b \rho_g C_{pg}}\frac{\partial^2 T}{\partial \zeta^2} \tag{S27}$$

Mass and energy balance in the solid phase:

$$\frac{\partial C_{i,s}}{\partial \tau} = (1 - \varepsilon_b) t_{res} r_i^s + k_{g,i} a_v t_{res}\left(C_i - C_{i,s}\right) \tag{S28}$$

$$\frac{\partial T_s}{\partial \tau} + \frac{h_f a_v (T_s - T) t_{res}}{\rho_{bed} C_{p,bed}} = \frac{(1 - \varepsilon_b) t_{res}}{\rho_{bed} C_{p,bed}} \sum \Delta H_{rxn,j} \eta_j R_j \tag{S29}$$

As written in the "section model" assumption of the main paper, we assume η_j is 1 in our model, but we keep this parameter in equation S29, so that this equation is also more generally valid, for other conditions.

As it is also mentioned in the main paper, the term $\frac{t_{res}}{\varepsilon_b} k_{g,i} a_v \left(C_i - C_{i,s}\right)$ in equations S26 and S28 represents the mass transfer between gas and solid phases, i.e., adsorption of the gas phase species on the catalyst surface. Therefore, it can be replaced by the adsorption rate for each species, that is calculated based on transition state theory in the surface model.

$$k_{g,i} a_v \left(C_i - C_{i,s}\right) = r_{ads} \tag{S30}$$

More information on this is given in the section **SI.2**.

Additionally, the term $\frac{h_f a_v t_{res}}{\varepsilon_b \rho_g C_{pg}}(T_s - T)$ in equations S27 and S29 represents the heat transfer between the bulk of the gas and the catalyst bed. In general, the temperature at the catalyst surface can be different from the bulk gas temperature. In the experiments to which our model is applied, the SEM micrographs before and after plasma showed no difference since the Pt catalyst was at a distance of 15 cm from the tail of the active plasma area. This was in good agreement with the minimal temperature increase (i.e., 1-2 ℃) that was experimentally observed at the catalyst surface upon plasma ignition [13], so the time dependency of the surface temperature ($\frac{\partial T_s}{\partial \tau}$) can be neglected. Therefore, the gas-solid heat transfer rate can analytically be calculated from equation 12 as follows:

$$h_f a_v (T_s - T) = (1 - \varepsilon_b) \sum \Delta H_{rxn,j} \eta_j R_j \tag{S31}$$

SI.4. Measured NO and calculated N_2, O_2, N and O concentrations entering the catalyst bed

The set of differential equations describing the catalytic system under study is very sensitive to the values set as initial and boundary conditions. This is specifically true for the NO and N post-plasma concentration, entering the catalyst bed. Therefore, selecting appropriate initial conditions is highly important for the model to predict reliable results. The post-plasma, as well as post-catalytic NO concentration is measured by Ma et al. [13] and their measured values as function of O_2 fraction in the feed gas are listed in table S2.

Table S2. Measured post-plasma and post-catalytic NO concentrations as a function of O_2 fraction in the feed gas [13].

x_{O_2}	$C_{NO}^{after\ plasma}$ (mol m^{-3})	$C_{NO}^{after\ catalyst}$ (mol m^{-3})
0.17×10^{-3}	1.53×10^{-7}	0.024×10^{-3}
0.35×10^{-3}	2.70×10^{-7}	0.049×10^{-3}
0.52×10^{-3}	4.13×10^{-7}	0.061×10^{-3}
0.7×10^{-3}	4.4×10^{-7}	0.059×10^{-3}
0.87×10^{-3}	5.73×10^{-7}	0.058×10^{-3}
1.04×10^{-3}	5.99×10^{-7}	0.055×10^{-3}
1.22×10^{-3}	6.12×10^{-7}	0.053×10^{-3}
1.39×10^{-3}	6.24×10^{-7}	0.052×10^{-3}
1.74×10^{-3}	5.59×10^{-7}	0.047×10^{-3}
2.09×10^{-3}	5.41×10^{-7}	0.042×10^{-3}
2.79×10^{-3}	5.13×10^{-7}	0.035×10^{-3}
3.48×10^{-3}	4.79×10^{-7}	0.027×10^{-3}
4.18×10^{-3}	4.12×10^{-7}	0.02×10^{-3}
5.57×10^{-3}	6.4×10^{-7}	0.013×10^{-3}
6.96×10^{-3}	8.74×10^{-7}	0.01×10^{-3}
0.01	29.12×10^{-7}	0.013×10^{-3}
0.014	68.56×10^{-7}	0.022×10^{-3}
0.017	0.13×10^{-4}	0.03×10^{-3}
0.021	0.23×10^{-4}	0.05×10^{-3}
0.035	0.75×10^{-4}	0.17×10^{-3}
0.1	1.94×10^{-4}	0.48×10^{-3}
0.15	2.15×10^{-4}	0.53×10^{-3}
0.2	2.21×10^{-4}	0.57×10^{-3}

Knowing the post-plasma concentration of NO, the estimated N radical concentration, and assuming that the O_2 dissociation fraction in plasma is normally one order of magnitude greater than for N_2 [26], [29]–[32], we can calculate the post-plasma concentration of each species, as described below.

Knowing the O_2 fraction in the feed gas, the N_2 fraction in the feed gas can be calculated as follows:

$$x_{N_2} = 1 - x_{O_2} \tag{S30}$$

Where x_{N_2} and x_{O_2} are the N_2 and O_2 mole fractions in the feed gas, respectively. Therefore the partial pressures of N_2 and O_2 in the feed gas can be calculated based on the total pressure, P_t, inside the plasma (i.e., 0.005 bar) as follows:

$$P_{N_2}^0 = x_{N_2} P_t \tag{S31}$$

$$P_{O_2}^0 = x_{O_2} P_t \tag{S32}$$

Clearly, the overall reaction of NO production ($N_2 + O_2 \leftrightarrow 2NO$), does not increase the pressure of the system. Therefore, the instantaneous total pressure, p, after dissociation of N_2 and O_2 in the plasma, given by the dissociation degrees g_{N_2} and g_{O_2}, respectively, is given by:

$$p = P_{N_2}^0\left(1 + g_{N_2}\right) + P_{O_2}^0\left(1 + g_{O_2}\right) \tag{S33}$$

The dissociation degrees are defined as $g_{N_2} = p_N / 2P_{N_2}^0$, and similar for O_2. The dissociation degree of O_2 is assumed 10 times higher than for N_2:

$$g_{O_2} = 10 g_{N_2} \tag{S34}$$

As the post-plasma concentration of NO is known from the experiments, its instantaneous partial pressure can be calculated as:

$$p_{NO} = C_{NO}^{ppm} p \times 10^{-6} \tag{S35}$$

Where C_{NO}^{ppm} is the measured post-plasma concentration of NO in ppm and the factor 10^{-6} is used to convert the ppm concentration into NO fraction. The instantaneous partial pressure of other species (i.e., N_2, O_2, N and O) after dissociation and conversion in the plasma can be calculated based on the assumed dissociation degrees and the instantaneous partial pressure of NO calculated based on its measured concentration, as follows:

$$\begin{aligned} p_{N_2} &= P_{N_2}^0 - \left(g_{N_2} P_{N_2}^0\right) - \left(\frac{p_{NO}}{2}\right) & \qquad p_{O_2} &= P_{O_2}^0 - \left(g_{O_2} P_{O_2}^0\right) - \left(\frac{p_{NO}}{2}\right) \\ p_N &= 2 g_{N_2} P_{N_2}^0 & \qquad p_O &= 2 g_{O_2} P_{O_2}^0 \end{aligned} \tag{S36}$$

From eq. S33 it is apparent that the pressure increases after dissociation. Therefore, we define a gas expansion factor, α, which enables us to calculate the post-plasma partial pressures of each species, while keeping the total pressure of the system constant (e.g., at 0.005 bar). The gas expansion factor can be calculated as follows:

$$\alpha = \frac{P_t}{p} \tag{S37}$$

As a result, the post-plasma partial pressure of each species, P_i, can be calculated as the product of the gas expansion factor and its corresponding instantaneous partial pressure as follows:

$$P_i = \alpha p_i \times 10^5 \tag{S38}$$

Where the factor 10^5 is used to convert the partial pressures from bar to Pa. Finally, the post-plasma concentration of each species, C_i (i.e., the initial conditions used in our model for the gas phase species, in units of mol m^{-3}) can be calculated using the ideal gas law as follows:

$$C_i = \frac{P_i}{RT_g} \tag{S39}$$

Where R and T_g are the gas universal constant and temperature, respectively.

SI.5. Dominant mechanisms toward NO production

In Fig. S2. we plot the reaction rates as a function of time of the main reactions leading to NO production, at different positions of the catalyst bed. The results are calculated at $x_{O_2} = 20\%$ (and $T_g = 873\ K, P = 5\ mbar, Q = 1.67 \times 10^{-6}\ m^3 s^{-1}$, N_2 dissociation fraction $= 3.5 \times 10^{-3}$) , which is one of the operating conditions for which the model was validated. An O_2 fraction of 20% was chosen, mimicking dry air composition, and therefore of special interest for industrial purposes.

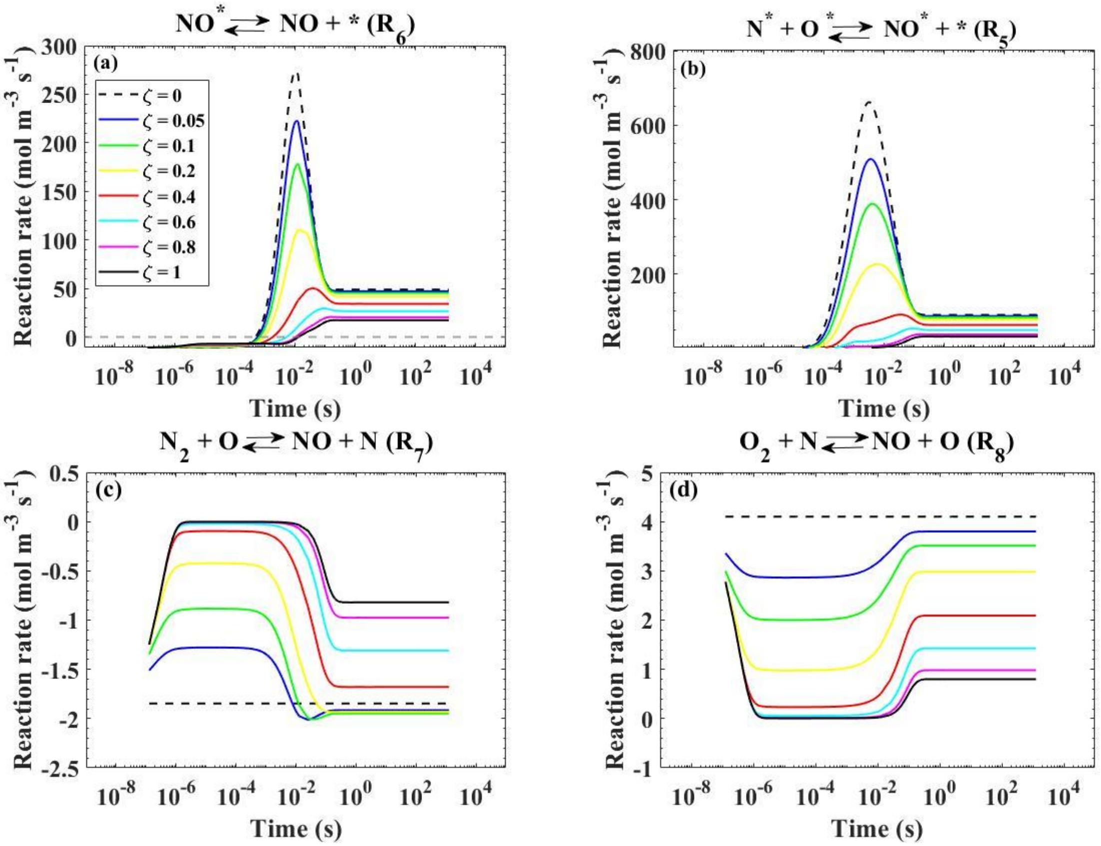

Figure S2. Temporal behavior of the net reaction rates of (a) NO desorption (R_6), (b) associative recombination of N^* and O^*radicals adsorbed at the catalyst surface (R_5), (c and d) the gas phase Zeldovich mechanisms (R_7, and R_8) at different positions across the catalyst bed (indicated in the legend by the dimensionless parameter ζ). To obtain a complete picture of the reaction mechanisms, the temporal behavior of the net rates of the other reactions are presented in section SI.7. Note that the reactions are written as equilibrium reactions; if the net rate is positive, the reaction proceeds in the forward direction; vice versa, when it is negative, it proceeds in the backward direction.

At time zero, when the post-plasma gas enters the catalyst bed, the active sites on the catalyst surface are all free and therefore, the species in the gas phase become adsorbed on the surface. As a consequence of adsorption of gas phase NO on the surface, the net rate of NO desorption (R_6) from the surface is negative at the startup of the process ($t < 10^{-3}$ s), until its surface concentration reaches the amounts that can push the equilibrium toward the desorption of NO from the surface (Fig. S2a). Due to the lack of N and O radicals on the catalyst surface in the beginning, the rate of associative recombination (R_5) is almost zero at the startup of the process (Fig. S2b). However, as soon as N and O radicals become adsorbed on the catalyst surface, they start to recombine to form NO. Therefore, the reaction rate of associative recombination (R_5) toward NO production on the surface starts to increase at around 10^{-4} s. Nevertheless, the NO desorption rate (R_6) rises a little bit later (around 10^{-3} s) as it takes some time for the NO concentration on the surface to be high enough to shift the equilibrium toward its desorption. As time passes, the rates of both associative recombination (R_5) and NO desorption (R_6) rise until they reach a maximum at $t \cong 10^{-2}$ s. At this maximum, the amount of produced NO through surface reactions is so high that it again promotes the adsorption of NO and its subsequent dissociation on the catalyst surface. Therefore, the net reaction rates of both associative recombination (R_5) and NO desorption (R_6) from the surface drop again until they reach a constant value at steady state ($t \geq 10^{-1}$ s). It should be noted that the associative recombination reaction (R_5), due to its lower activation energy (cf., table 2), is always faster than NO desorption (R_6) (cf. Fig. S2a and S2b).

A detailed analysis of the concentration and net reaction rate of each species in the gas phase in the catalytic bed and at the catalyst surface as a function of time and at different positions across the catalyst bed is presented in sections **SI.6** and **SI.8**. In addition, analysis of the heat transfer in the catalyst bed is presented in section **SI.9**. According to Fig. S3a, the gas phase NO concentration rises in the axial direction. Simultaneously, a drop is observed in the axial direction for the surface concentrations of NO^*, N^*, and O^* (cf., Fig. S3b, S3d, and S3g, respectively). The rise in the gas phase concentration of NO in the axial direction, promotes its adsorption on the surface. This, in addition to the drop in the concentrations of N^*, and O^*, which results in a drop in the net rate of associative recombination (R_5) in the axial direction (cf. Fig. S2b), also leads to a drop in the net rate of NO desorption (R_6) from the surface in the axial direction (cf. Fig. S2a).

Besides the associative recombination of N and O radicals at the catalyst surface and the subsequent desorption of the produced NO from the catalyst surface, which are the most important NO production mechanisms (cf. their high reaction rates), NO can also be produced in the gas phase by the so-called Zeldovich reactions. However, the rates of these reactions are much lower, as can be observed from Fig. S2c and S2d.

The temporal behavior of the first Zeldovich reaction (R_7) is shown in Fig. S2c. It is clear that this reaction favors NO consumption throughout the whole period of the process. When the post-plasma gas flows into the catalyst bed, at first the reaction rate starts to increase until it reaches a maximum at around 10^{-6} s, after which its net rate stays constant until around 10^{-2} s. Subsequently, the net reaction rate drops again until it reaches a constant value at steady state (at around 0.1 s). The second Zeldovich reaction (R_8) on the other hand, experiences the opposite behavior (Fig. S2d). When the post-plasma gas enters the catalyst bed, the net rate of this reaction starts to drop at $t < 10^{-6}$ and it reaches a minimum at around 10^{-6} s, after which its net rate stays constant until around 10^{-2} s, when the net rate starts to slightly increase again, until it reaches a constant value at steady state (at around 0.1 s). Note that, because the concentrations of all the gas phase species are constant at the inlet of the catalyst bed (i.e., they are equal to the post-plasma concentrations of species entering the catalyst bed) the net reaction rate of both Zeldovich reactions, at the inlet of the catalyst bed, (i.e., $\zeta = 0$) is constant throughout the whole period of the process.

According to Fig. S2c, the first Zeldovich reaction (R_7) favors the NO consumption throughout the whole period of the process, as well as in the axial direction. In contrast, the second Zeldovich reaction (R_8) always favors the NO production, both as function of time and position across the catalyst bed (cf., Fig. S2d). The drop in the gas phase concentration of N radicals in the axial direction (cf., Fig. S3c) slows down the rate of backward and forward pathways of the first and second Zeldovich reactions (R_7, R_8), respectively. As a result, we observe a rise (i.e., becoming less negative) and a drop (i.e., becoming less positive) in the net rate of the first and second Zeldovich reaction (R_7, R_8) in the axial direction, respectively.

In general, the total rate of both gas phase Zeldovich mechanisms (R_7, R_8) acts in favor of NO production (i.e., the sum of the net rate of both reactions is positive at steady state, meaning that they proceed towards NO production). However, the gas phase Zeldovich reactions play a negligible role, compared to the surface reactions (R_5, R_6) towards NO production. Indeed, this is obvious when comparing the net reaction rates of surface reactions that are in average between 1-2 orders of magnitude higher than those of gas phase Zeldovich reactions. This clearly indicates that the presence of the catalyst helps to significantly improve the NO production at the conditions under study.

SI.6. Species concentrations to explain the NO production mechanisms

To better understand the temporal and spatial behavior of the reaction rates and how the presence of the catalyst helps to improve the process, we plot in Fig. S3 the concentrations of all the species, both in the gas phase and at the catalyst surface, as a function of time at different positions in the catalyst bed.

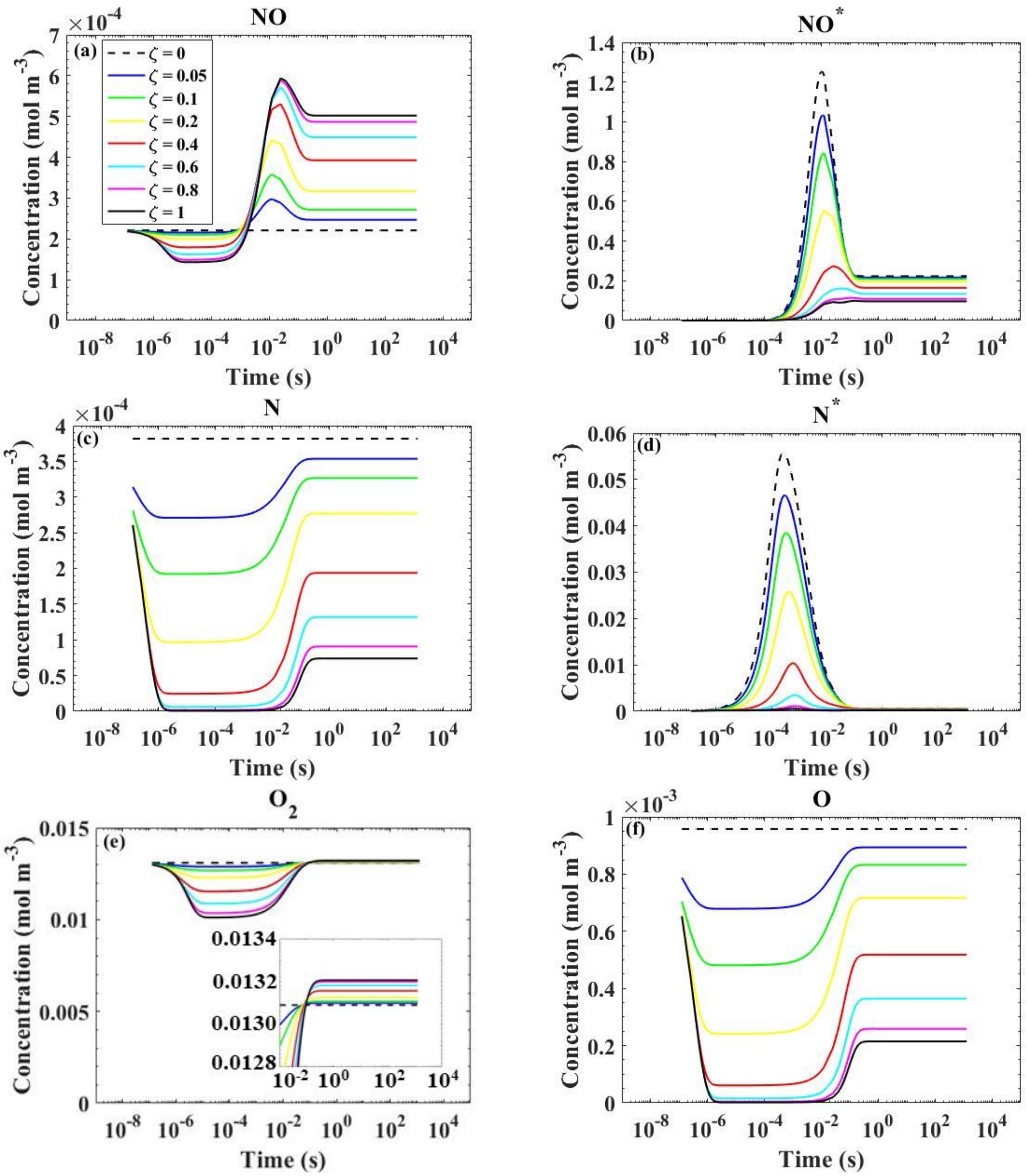

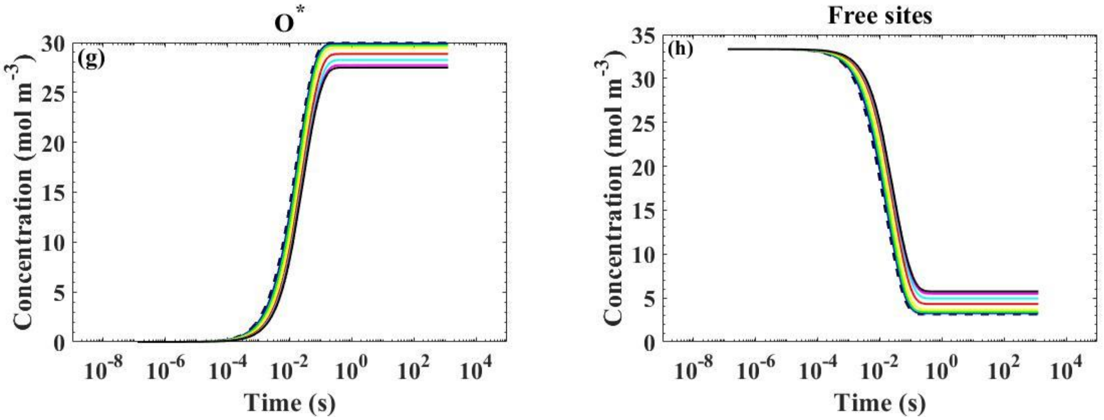

Figure S3. Temporal behavior of the concentrations of the system's different species in the gas phase (a, c, e, f) and at the catalyst surface (b, d, g, h) at different positions across the catalyst bed (indicated in the legend by the dimensionless parameter, $\zeta = \frac{z}{L}$). $x_{O_2} = 20\%, T_g = 873\ K, P = 5\ mbar, Q = 1.67 \times 10^{-6}\ m^3s^{-1}, T_v = 6000\ K.$, N_2 dissociation fraction $= 3.5 \times 10^{-3}$

When the post-plasma gas enters the catalyst bed, some of the NO molecules already formed in the plasma are quickly adsorbed on the catalyst surface (the adsorption of NO on the surface is barrierless, cf., table 2 in the main paper). Therefore, a slight initial decrease in the gas phase NO concentration is observed ($t < 10^{-4}$ s, Fig. S3a). As time passes and the gas flows through the catalyst bed, the rate of associative recombination reaction (R_5) becomes more and more dominant due to adsorption of N and O radicals on the surface, starting at around 10^{-4} s (Fig S2b). As a result, the NO concentration on the catalyst surface increases (Fig. S3b) until the NO adsorption/desorption process (R_6) shifts toward its desorption from the surface (at around 10^{-3} s, Fig. S2a), and the NO concentration on the catalyst surface starts to drop, until it reaches a constant value at steady state (at around 0.1 s, Fig. S3b). Subsequently, the NO concentration in the gas phase gradually increases, until it reaches a maximum at around 10^{-2} s (Fig. S3a). At this maximum the NO concentration in the gas phase slightly drops again, until it reaches constant steady state value as well at around 0.1 s (Fig. S3a). The reason is that the amount of produced NO through surface reactions, and its subsequent desorption from the surface, and therefore its gas phase concentration is high enough to promote its adsorption on the catalyst surface. As a result, the net rate of NO desorption (R_6) decreases.

Adsorption of N radicals on the surface (R_3) is a barrierless process. When the post-plasma gas enters the catalyst bed, the gas phase N radicals quickly adsorb on the free active catalyst sites. Therefore, the N radical gas phase concentration drops, until around 10^{-6}s, (Fig. S3c) and its concentration increases on the catalyst surface (Fig. S3d) until it reaches a maximum at around 10^{-4} s. At this maximum, due to the high concentration of N radicals on the catalyst surface, the associative desorption reaction (R_1) of N radicals on the catalytic surface gets promoted (cf., Fig. S4a) and the concentration of N_2 in the gas phase slightly increases (not shown in Fig. S3, because the effect is barely visible). This, in addition to the contribution of N radicals in the associative recombination reaction (R_5) and its direct desorption from the catalyst surface (R_3), results in a drop of N radicals on the surface after the maximum is reached (10^{-4} s). Finally, as a consequence of direct desorption of N radicals from the catalyst surface, the N radical concentration in the gas phase starts to increase again at around 10^{-2} s until it reaches steady state (0.1 s).

Additionally, the temporal behavior of the N radical gas phase concentration also affects the behavior of the gas phase Zeldovich mechanisms. The drop in the gas phase concentration of N radicals at around 10^{-6} s slows down the backward pathway of the first Zeldovich and the forward pathway of the second Zeldovich reactions (R_7, and R_8, respectively). As a result, the first and second Zeldovich reaction rates exhibit a rise and drop, respectively (Fig. S2c and S2d). During the period in which the gas phase concentration of N radicals is constant (i.e., until around 10^{-2} s), the net rate of both Zeldovich reactions also stays constant. After this period, when the N radical gas phase concentration slightly increases at around 10^{-2} s, the first and second Zeldovich reaction rates are again characterized by a drop and a rise, respectively, until their net rate reaches a constant value at steady state (around 0.1 s), when the gas phase concentration of N radicals also reaches a constant value. Furthermore, this drop in the net rate of the first Zeldovich reaction (Fig. S2c) also contributes to the slight increase in the concentration of N_2 in the gas phase until it reaches a constant value at steady state (0.1 s).

Simultaneously, due to a very low energy barrier for O_2 dissociative adsorption (i.e., 0.17 eV, R_2) and zero energy barrier for O radical adsorption (cf., R_4 in table 2), the concentrations of both O_2 and O radicals in the gas phase decrease over time (Fig. S3e and S3f), and the concentration of O radicals on the surface dramatically increases (Fig. S3g). As time passes, the surface gets more and more covered by O radicals, and at steady state, almost all of the catalyst active surface sites are covered by O radicals (cf. the opposite profiles of Fig. S3g and S3h). As a result, when steady state is reached, the associative desorption of O radicals (R_2) as well as its direct desorption (R_4) from the catalyst surface become the dominant mechanisms within the system, due to the very high concentration of O radicals on the surface (cf., Fig. S4 c and S4d). Therefore, the concentrations of both O_2 and O in the gas phase increase again through O radical associative desorption and direct desorption from the surface, respectively (Fig. S3e and S3f) and they reach constant values at steady-state (around 0.1 s).

The spatial behavior of the species concentrations across the catalyst bed, which also explains the spatial behavior of the NO production reactions, is explained in detail in section **SI.8**, where we plot the production and loss rates of all the species, both in the gas phase and at the catalyst surface, as a function of axial position in the catalyst bed.

SI.7. Temporal behavior of the net reaction rates at different positions across the catalyst bed

In **SI.5**, we plotted the rates of the main reactions leading to NO production as a function of time, at different positions of the catalyst bed, i.e., reactions R_5, R_6, R_7 and R_8. To obtain a complete picture of the reaction mechanisms, the temporal behavior of the net reaction rates for N_2 and O_2 dissociative adsorption (R_1 and R_2), as well as N and O radical adsorption on the surface (R_3 and R_4) are presented in Fig. S4.a-d. At the startup of the process, almost no dissociative adsorption of N_2 on the catalyst surface (R_1) happens, due to its very high activation energy barrier, and its net rate stays almost zero until around 10^{-6} s (Fig. S4.a). As the concentration of N radicals on the catalyst surface starts to increase (at around 10^{-6} s, Fig. S3d), due to its fast adsorption on the surface (N radical adsorption is a barrierless process, cf., table 2 in the main paper), associative desorption of N radicals gets promoted, and therefore, the net rate of N_2 dissociative adsorption (R_1) is negative until it reaches a minimum at around 10^{-4} s. Between 10^{-4} and 10^{-2} s, due to the higher rate of associative recombination on the surface (R_5) and direct desorption of N radicals from the surface, the rate of associative desorption of N radicals from the surface decreases and therefore, the net rate of N_2 dissociative adsorption (R_1) increases (i.e., becomes less negative) until it goes back to zero at steady state (around 0.1 s).

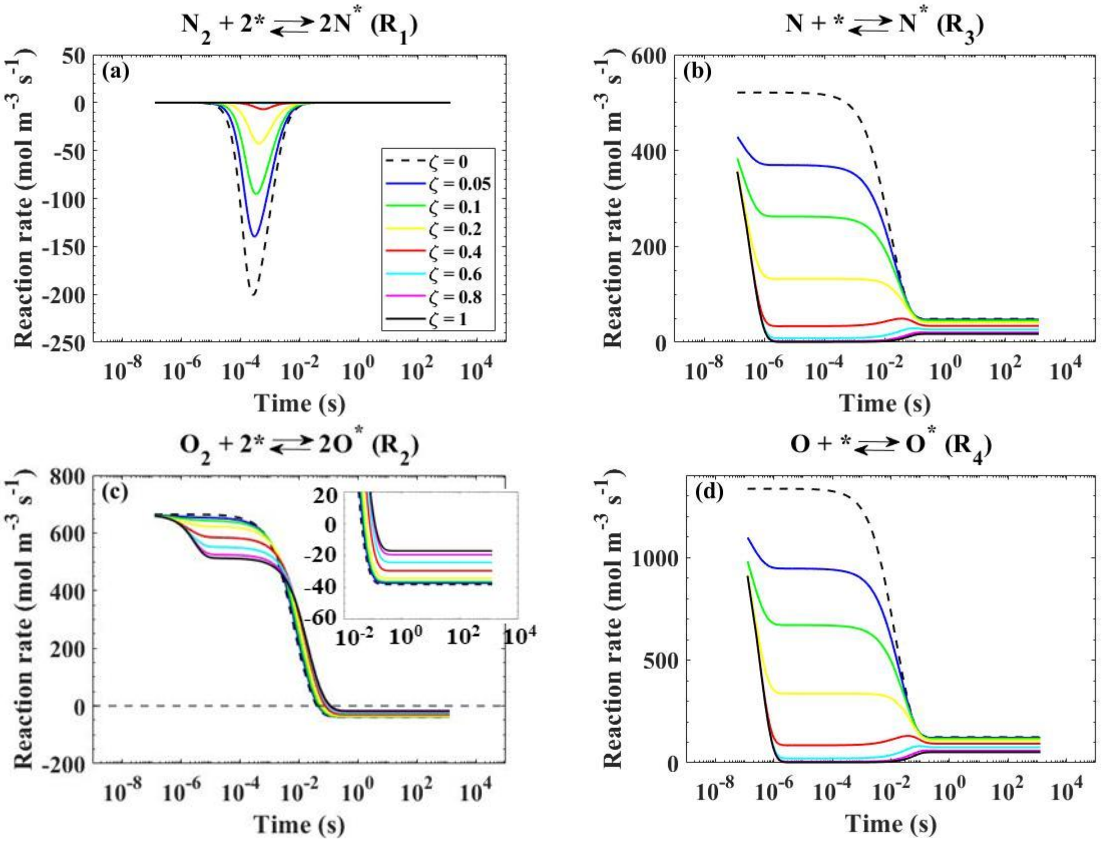

Figure S4. Temporal behavior of the net reaction rate of (a) dissociative adsorption of N_2 (R_1), (b) N radical adsorption (R_3), (c) dissociative adsorption of O_2 (R_2), and (d) O radical adsorption (R_4), at different positions across the catalyst bed (indicated in the legend by the dimensionless parameter $\zeta = \frac{z}{L}$). $x_{O_2} = 20\%, T_g = 873\ K, P = 5\ mbar, Q = 1.67 \times 10^{-6}\ m^3 s^{-1}, T_v = 6000\ K, N_2$dissociation fraction $= 3.5 \times 10^{-3}$

At the startup of the process, the N radical adsorption (R_3) on the surface occurs at a relatively high rate (Fig. S4.b). However, as a result, its concentration in the gas phase decreases until around 10^{-6}s. Therefore, the net rate of this process decreases until around 10^{-6} s. Between 10^{-6} and 10^{-3}s, the concentration of N radicals in the gas phase stays constant and therefore, their net rate of adsorption on the surface also stays constant. From 10^{-3}s the enhanced direct desorption of N radicals from the surface, due to their higher surface concentration, results in a lower net rate of N radical adsorption (R_3) on the surface, until it reaches a constant value at steady state (at around 0.1 s).

Due to a very low energy barrier for O_2 dissociative adsorption (i.e., 0.17 eV reaction barrier for R_2), and the high concentration of O_2 in the gas phase, this process occurs with high rates at the startup of the process (Fig. S4.c). As a result of the drop in concentration of O_2 in the gas phase until 10^{-5} s, the net rate of O_2 dissociative adsorption drops. As the concentration of O_2 in the gas phase stays almost constant until around 10^{-3} s (Fig. S3e), almost no variation is observed in the net rate of O_2 dissociative adsorption. Starting from 10^{-3} s, the dramatic increase in the surface concentration of O radicals (Fig. S3g), increases the rate of their associative desorption from the surface, and the net rate of O_2 dissociative adsorption (R_2) drops significantly until it reaches a constant negative value at steady state (around 0.1 s), meaning that when steady state is reached, no O_2 dissociative adsorption occurs in the catalyst bed and the process mostly works in favor of associative desorption of O radicals from the surface.

Finally, as O radical adsorption is a barrierless process (cf., table 2 in the main paper for R_2), this process occurs with very high rates at the startup of the process, due to the relatively high concentration of O radicals in the post-plasma gas entering the catalyst bed (Fig. S4.d). The drop in the concentration of O radicals in the gas phase until 10^{-6} s results in a drop in the net rate of the O radical adsorption (R_2). From 10^{-6} to around 10^{-3} s the concentration of O radicals in the gas phase stays constant and therefore no variations in the net rate of O radical adsorption (R_2) is observed. Starting from 10^{-3} s, the rate of direct desorption of O radicals from the surface increases, due to the dramatic rise of their surface concentration, which results in a significant drop in the net rate of O radical adsorption (R_2) until it reaches a constant value at steady state (around 0.1 s).

SI.8. Species formation and loss rates in the axial direction

A big advantage of our model is that it provides information on the axial profiles of the species concentrations and reaction rates, which can give more insight in the actual mechanisms. Therefore, in this section we plot the steady state production and loss rates of each species as a function of dimensionless position ($\zeta = \frac{z}{L}$) across the catalyst bed in Fig. S5.

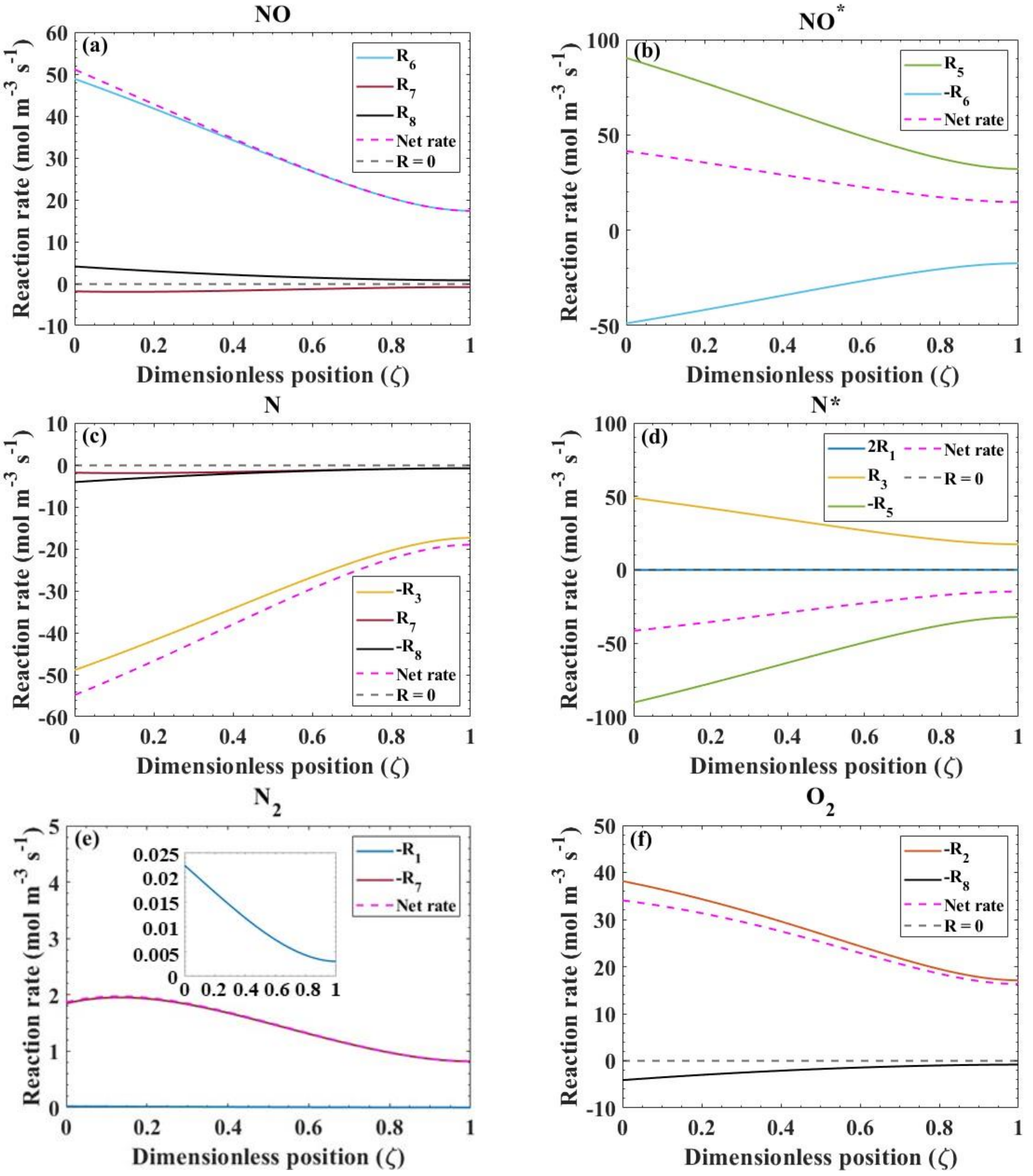

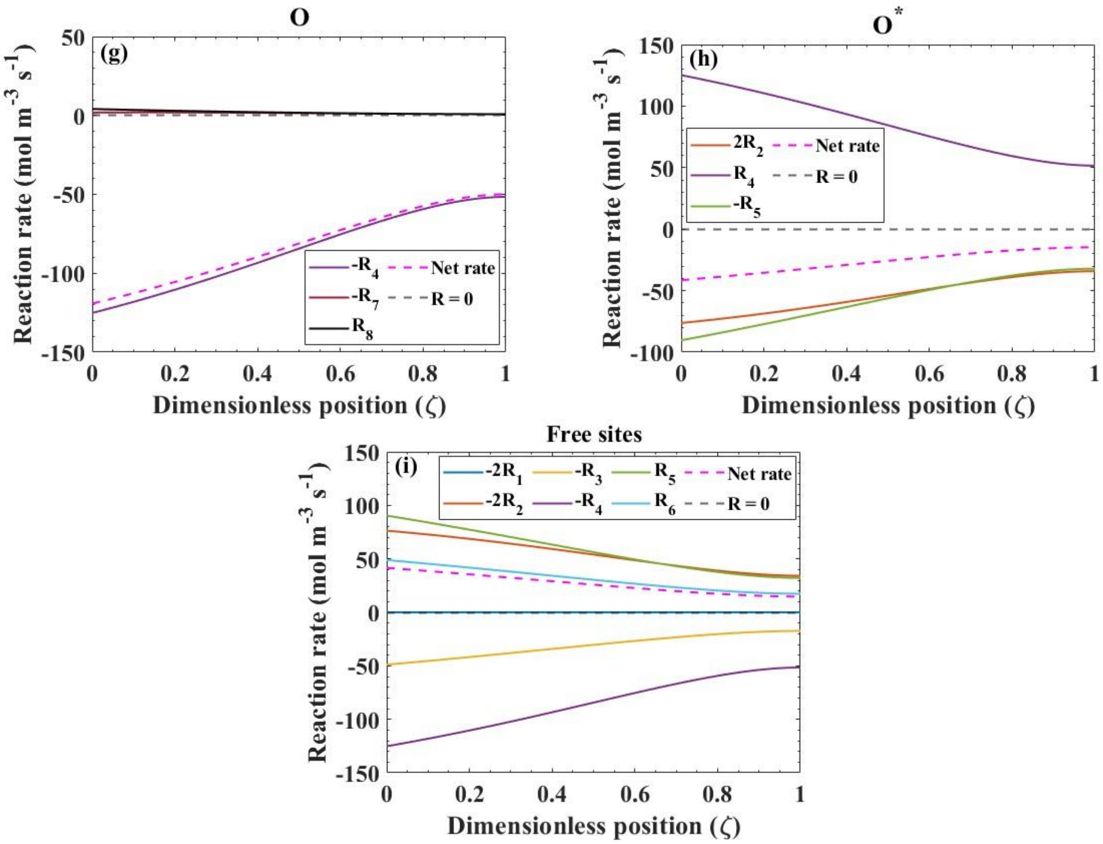

Figure S5. Axial profiles of the various production and loss rates of the different species in the gas phase (a, c, e, f, g), and on the catalyst surface (b, d, h, i) as a function of dimensionless position (ζ) from the catalyst bed inlet at $x_{O_2} = 20\%, T_g = 873\ K, P = 5\ mbar, Q = 1.67 \times 10^{-6}\ m^3s^{-1}, T_v = 6000\ K, N_2$ dissociation fraction $= 3.5 \times 10^{-3}$. A positive or negative reaction rate stands for production and loss, respectively. A negative sign for "R" in the legend represents the consumption of a species through the reaction listed in table 2 or 3.

As observed by Ma et al. [13] both experimentally and through their model, the coupled plasma and catalyst promotes the process towards higher overall production of NO. Additionally, we showed in **SI.5** (Fig. S2), that in such a system the mechanisms happening due to the presence of the catalyst have much higher rates than the gas phase Zeldovich reactions (R_7 and R_8). The rate of production or destruction of NO through different mechanisms in the axial direction of the catalyst bed is shown in Fig. S5a. As can be seen, in the gas phase, NO is consumed through the first Zeldovich reaction (R_7) and it is produced through the second Zeldovich reaction (R_8), but by far the most important production is by desorption from the catalyst surface (R_6). The same effect was observed by Ma et al. [13]. As the net production rate of NO is always positive throughout the whole catalyst bed, its gas phase concentration increases across the catalyst bed (Fig. S3a). However, as we get closer to the outlet of the catalyst bed, a drop in the NO net production rate is observed (see Fig. S5a). The reason is the drop in the net rate of NO desorption (R_6), due to the lower surface concentration of NO in the axial direction (Fig. S3b), which is the most important mechanism that controls the net production rate of NO in the gas phase.

At the catalyst surface, NO is produced through associative recombination (R_5), and it is consumed through desorption from the surface (R_6). The NO desorption, due to its higher energy barrier (cf., table 2), is always slower than its production on the catalyst surface through associative recombination (R_5). As a result, the net production rate of NO on the catalyst surface is always positive (Fig. S5b). As the flowing gas gets closer to the outlet of the catalyst bed, the rates of both recombination (R_5) and desorption (R_6) decrease.

As the NO desorption from the surface (R_6) is the mechanism that controls the net NO production rate in the gas phase (Fig. S5a), its decrease results in a drop of the net rate of NO production across the catalyst bed.

In the gas phase the N radicals are consumed through the Zeldovich mechanism (R_7 and R_8), but especially by adsorption on the catalyst surface (R_3). Therefore, the net rate of the N radicals is always negative (i.e., they are always consumed) throughout the catalyst bed (Fig. S5c). As a result, their gas phase concentration decreases as the flowing gas gets closer to the outlet of the catalyst bed (Fig. S3c). The drop in gas phase concentration of N radicals in the axial direction slows down their adsorption. Therefore, their net consumption rate becomes lower as the gas approaches the outlet of the catalyst bed.

As can be seen in Fig. S5d, on the catalyst surface, the N radicals are produced through adsorption from the gas phase (R_3) as well as N_2 dissociative adsorption (R_1), although the latter turns out to be negligible due to a very high energy barrier. Simultaneously, it is consumed through associative recombination (R_5). As dissociative adsorption on the surface is negligible, the production of N radicals on the surface is only controlled by the amount of N radicals produced by the plasma that adsorb on the catalyst surface. At the same time, at steady state the surface is mostly covered by O radicals (Fig. S3g). As a result, as soon as N radicals are adsorbed on the catalyst surface, they quickly react with the O radicals on the surface and form NO through associative recombination (R_5). Hence, the rate of associative recombination (R_5) is always higher than N radical adsorption (R_3). Therefore, the net rate of N radicals on the catalyst surface is always negative (i.e., they are always consumed) throughout the catalyst bed, which leads to a drop in their concentration on the catalyst surface in the axial direction (Fig. S3d).

N_2 is produced through associative desorption of N radicals from the catalyst surface (R_1), as well as the first Zeldovich reaction (R_7). As a result, its net rate is always positive (i.e., it is produced, Fig. S5e), and its concentration increases throughout the catalyst bed. However, at steady state, the rate of the first Zeldovich reaction (R_7) is much higher than that of associative desorption of N radicals from the surface (R_1). As the flowing gas gets closer to the catalyst bed outlet, the amount of N radicals decreases both in the gas phase and on the catalyst surface (Fig. S3c and S3d). Therefore, the rates of both associative desorption of N radicals from the surface (R_1) and the first Zeldovich reaction (R_7) drop closer towards the catalyst bed outlet.

Simultaneously, O_2 in the gas phase is produced through associative desorption of O radicals (R_2) and it is consumed through the second Zeldovich reaction (R_8). However, the effect of the latter is much smaller than for associative desorption (R_2). As a result, the net rate of O_2 in the gas phase is always positive (i.e., it is produced, Fig. S5f), and its steady state concentration increases throughout the catalyst bed (Fig. S3e).

In the gas phase, O radicals are produced by the reverse process of the first Zeldovich reaction and by the forward second Zeldovich reaction (R_7, R_8), and consumed through direct adsorption on the catalyst surface (R_4). The latter reaction is much more important, and therefore, the net rate of O radicals in the gas phase is always negative (i.e., it is always consumed, Fig. S5g), and thus, its concentration decreases throughout the catalyst bed (Fig. S3f). The drop in the amount of O radicals in the gas phase at positions closer to the catalyst bed outlet results in a drop in its adsorption rate on the surface and subsequently its net rate decreases.

At the catalyst surface, O radicals are produced through adsorption from the gas phase (R_4) and consumed through associative desorption from the surface (R_2) as well as associative recombination with N radicals (R_5) on the catalyst surface (Fig. S5h). The rate of O radicals on the catalyst surface is controlled by their consumption mechanisms, hence, their net rate is always negative (i.e., they are consumed), and their concentration decreases towards the outlet of the catalyst bed (Fig. S3g).

According to Fig. S5h, the rate of O radical adsorption (R_4) is 3-3.6 times higher than its net rate of consumption, as well as that of N radical adsorption on the catalyst surface (Fig. S5c). This results in accumulation of O radicals on the catalyst surface in steady state. This, in addition to the lower amount of N radicals on the catalyst surface at positions closer to the outlet of the catalyst bed, as well as NO desorption from the surface, results in a lower steady state surface concentration of NO in the axial direction (Fig. S3b).

All the surface reactions in table 2 affect the active free sites on the catalyst surface as well (Fig. S5i). More free surface sites become available through associative recombination (R_5), associative desorption of O radicals (R_2), and NO desorption from the surface (R_6). At the same time, the surface sites become occupied through N and O radical adsorption (R_3, R_4, respectively). As the sum of the production rates of free active sites is greater than the sum of their consumption rates, the net rate of free active sites stays positive throughout the catalyst bed. As the O radicals are the dominant species that cover the free catalyst sites, the drop in their concentration in the axial direction results in a larger amount of active free sites at the catalyst surface (Fig. S3h).

SI.9. Heat transfer analysis

Our model also accounts for the heat transfer in the catalyst bed. Therefore, in this section we present a detailed heat transfer analysis to investigate the temporal and spatial behavior of gas phase temperature inside the catalyst bed. The temporal behavior of the net heat flux in the system and the gas temperature, at different positions of the catalyst bed, is presented in Fig. S6a and S6b. Additionally, to better understand the behavior of gas temperature across the catalyst bed, the steady state heat fluxes due to each reaction, as well as the net heat flux of the whole process as a function of dimensionless position, are shown in Fig. S6c.

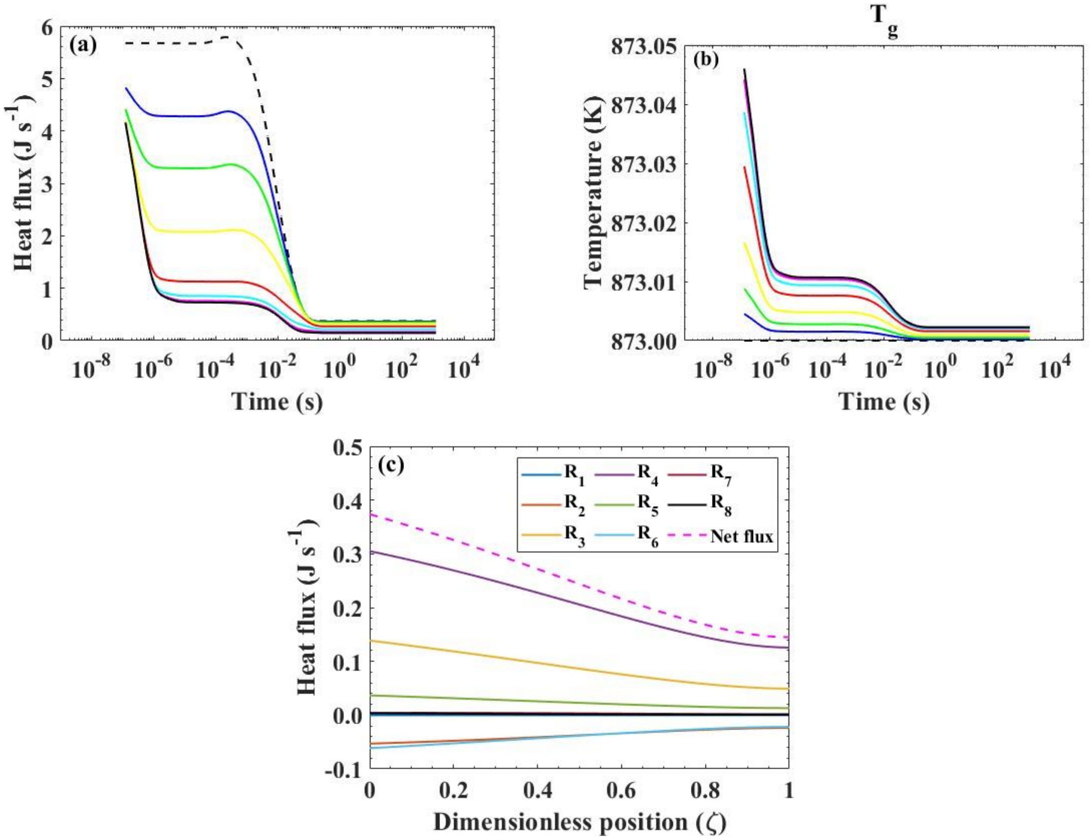

Figure S6. Net heat flux in the system (a), and gas temperature (b) as a function of time at different positions across the catalyst bed, and steady state heat flux due to each reaction, as well as the net heat flux of the system (c) as function of dimensionless position ($\zeta = \frac{z}{L}$) from the catalyst bed inlet at $x_{O_2} = 20\%, T_g = 873\ K, P = 5\ mbar, Q = 1.67 \times 10^{-6}\ m^3 s^{-1}, T_v = 6000\ K, N_2$ dissociation fraction $= 3.5 \times 10^{-3}$.

At the startup of the process ($t < 10^{-6}$ s), heat is released through all the reactions, except by dissociative adsorption of N_2 (R_1) and associative recombination of N and O radicals at the surface (R_5), as their rate at the process startup is almost zero. Therefore, a considerable heat flux is observed at the startup of the process (Fig, S6a). However, the net heat flux drops quickly until around 10^{-6} s, due to the drop in the rate of heat released in the reactions. In the time interval from 10^{-6} to around 10^{-2} s, the dissociative adsorption of N_2 (R_1) first starts to release heat until around 10^{-4} s, as it proceeds in the backward direction. Afterwards, the released heat by this reaction drops until it again becomes zero at around 10^{-2}, when its net rate becomes zero again (Fig. S5a). During this period of time, the rate of dissociative adsorption of O_2 (R_2) drops (Fig. S5c), and as a result, the released heat through this reaction drops as well. Simultaneously, the net rates of adsorption of N and O radicals (R_3 and R_4) and of the gas phase Zeldovich mechanism (R_7

and R_8) stay constant (Fig. S4b and S4d, and Fig. S2c and S2d, respectively), and therefore the released heat from these reactions stays constant. The rise in the rate of associative recombination (R_5) results in an increase in heat released by this reaction (Fig. S2b). Finally, due the increase of the rate of NO desorption (R_6) from the catalyst surface, this process gradually becomes heat absorbing (Fig. S2a). In general, the variation in the released or absorbed heat by different reactions in the system is such that it keeps the net heat flux constant in the time period from 10^{-6} to around 10^{-2} s. Afterwards, the net heat flux of the system decreases again, due to the lower net rate of heat-releasing reactions until it reaches a constant value at steady state (around 0.1 s).

Due to the considerable heat flux (Fig. S6a) at the startup of the process ($t < 10^{-6}$ s), the gas temperature slightly increases (Fig. S6b). As time passes (until around 10^{-6} s) the gas temperature decreases again due to the drop in the net heat flux of the system, but still its temperature is slightly higher than its temperature at the inlet of the catalyst bed. During the period that the net heat flux of the system stays at a constant value (i.e., from 10^{-6} s to $t < 10^{-2}$ s), the gas temperature also stays constant. Afterwards, the gradual drop in the net heat flux of the system until it reaches a constant value at steady state (around 0.1 s), results in a drop in the gas temperature until it reaches a constant value at steady state. Overall, the gas temperature in the system is always negligibly higher than its temperature at the outlet of the reactor. The reason is that the net heat flux of the system is always positive throughout the whole catalyst bed. However, the increase in the temperature is so small that the whole process can be considered isothermal (cf., the small variation in y-axis in Fig. S6b).

Throughout the whole catalyst bed, at steady state, heat is absorbed through associative desorption of O radicals from the surface (R_2) and through NO desorption (R_6). The other reactions release heat throughout the whole catalyst bed (Fig. S6c). However, the heat released through dissociative adsorption of N_2 (R_1), and the gas phase Zeldovich mechanism (R_7 and R_8), is negligible compared to the released heat through the adsorption of N and O radicals (R_3 and R_4) and associative recombination (R_5). The net heat flux throughout the catalyst bed is controlled by heat releasing reactions, as they release more heat compared to the heat absorbed by the associative desorption of O radicals from the surface (R_2) and the NO desorption process (R_6). As a result, the net heat flux of the system of reactions is always positive throughout the catalyst bed. Therefore, the gas temperature slightly increases in the axial direction (Fig. S6b). Additionally, due to the drop in rate of all the reactions in the axial direction, the amount of released heat decreases closer to the catalyst bed outlet.

SI.10. Effect of the catalyst bed characteristics length on the contact time of the gas with the catalyst, as well as surface and gas phase reactions

in Fig. S7a, we plot the effect of catalyst bed characteristic length on the contact time of the gas with the catalyst. An increase in the catalyst bed characteristic length results in a linear increase in the total volume of the catalyst bed. As a result, the contact time of the gas with the catalyst linearly increases with increasing catalyst bed characteristic length (cf., the relationship of the catalyst bed characteristic length with total volume of the catalyst bed and the contact time of the gas with catalyst in table 1 of the main paper).

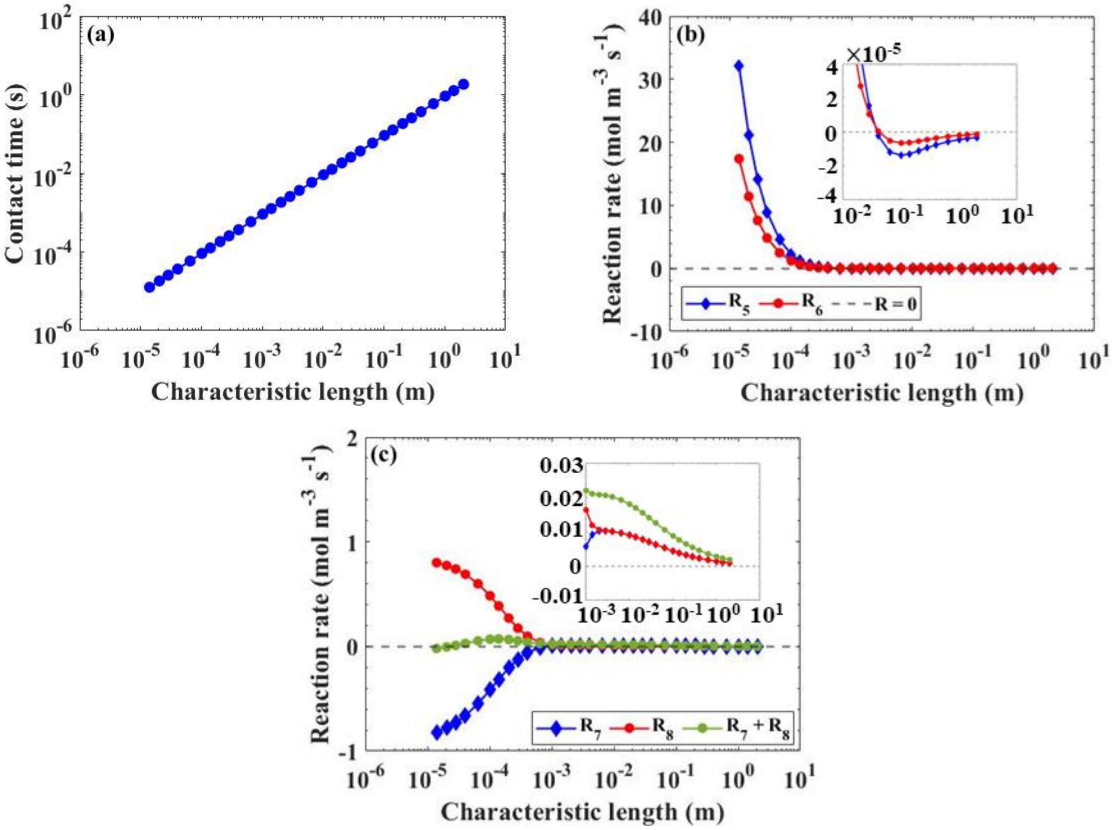

Figure S7. Effect of the catalyst bed characteristic length on (a) the contact time of the gas with the catalyst, (b) the net reaction rate of associative recombination of N and O radicals on the surface and NO desorption from the surface (R_5 and R_6), and (c) the net reaction rate of the gas-phase Zeldovich mechanisms (R_7 and R_8) and sum of both.

As the characteristic length of the catalyst bed increases, the net rate of associative recombination (R_5) and subsequent desorption of the produced NO (R_6) decrease dramatically, due to the enhanced NO adsorption on the surface and its subsequent dissociation into N and O radicals on the catalyst surface. This drop is that much that at characteristic lengths around 0.05 m and longer, not only the surface reactions have no contribution in NO production, but also the surface processes proceed toward NO destruction (cf., inset in Fig. S7b).

A higher rate of NO adsorption and its subsequent dissociation on the surface, due to an increase in the catalyst bed characteristic length, results in a lower net reaction rate of N and O radical adsorption (R_3 and R_4, respectively) through their desorption from the catalyst surface. It is also observed in section **SI.6** that at steady state the catalyst surface is mostly covered by O radicals and the O radical direct desorption is one of the dominant mechanisms. Therefore, the concentration of O radicals in the gas phase increases due to the higher rate of its direct desorption. The higher concentration of O radicals in the gas phase promotes the first Zeldovich reaction (R_7) towards production of NO, and as a result its net rate increases with increasing catalyst bed characteristic length (Fig. S7c). The net rate of the second Zeldovich reaction (R_8) on the other hand, decreases due to the promotion of its backward reaction as a result of the higher concentration of O radicals in the gas phase. However, its net rate stays toward NO production in the whole studied range of catalyst bed characteristic length (Fig. S7c).

Comparing the net reaction rate of NO desorption from the surface and the net reaction rate of gas phase Zeldovich reactions (green curve in Fig. S7c), we can observe that at low catalyst bed characteristic lengths ($< 10^{-4}$), the surface reactions are the dominant mechanisms that are controlling the NO production. However, at longer catalyst bed characteristic lengths, the gas phase Zeldovich reactions are the mechanisms that keep the process in favor of NO production, due to their higher net reaction rate.

SI.11. Effect of catalyst bed diameter on the porosity and characteristic length of the catalyst bed

We plot the characteristic length and the porosity of the catalyst bed as a function of catalyst bed diameter in Fig S8. a and b, respectively. Increasing the diameter of the catalyst bed results in a higher catalyst bed cross section area, and thus the catalyst bed characteristic length decreases (Fig. S8a; cf., the relationship of the catalyst bed characteristic length with the cross-section area of the catalyst bed in table 1 of the main paper). The drop in characteristic length of the catalyst bed, due to the larger diameter of the catalyst bed, results in a smaller total volume of the catalyst bed (cf., table 1 of the main paper for the relationship between the total volume of the catalyst bed and catalyst bed characteristic length), and therefore, the catalyst bed porosity drops (Fig. S8b; see also eq. S11 in SI.1 above).

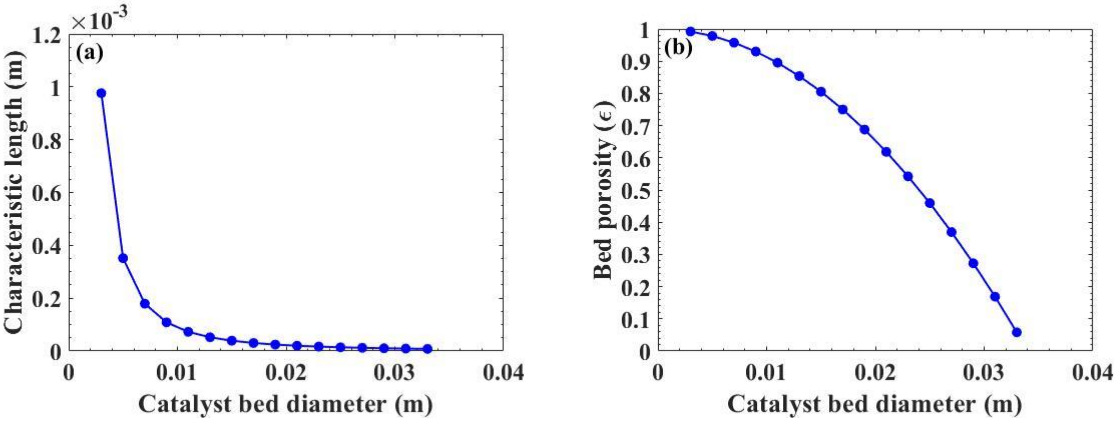

Figure S8. Effect of catalyst bed diameter on (a) characteristic length, and (b) porosity of the catalyst bed.

References

[1] S. Z. Abbas, V. Dupont, and T. Mahmud, “Kinetics study and modelling of steam methane reforming process over a NiO/Al2O3 catalyst in an adiabatic packed bed reactor,” *Int. J. Hydrogen Energy*, vol. 42, pp. 2889–2903, 2017, doi: 10.1016/j.ijhydene.2016.11.093.

[2] C. J. Geankoplis, “Transport processes and unit operations,” *The Chemical Engineering Journal*, vol. 20, p. 82, 1993, doi: 10.1016/0300-9467(80)85013-1.

[3] A. KoLodziej and J. Lojewska, “Engineering Aspects of Catalytic Converters Designs for Cleaning of Exhaust Gases,” *New Futur. Dev. Catal. Catal. Remediat. Environ. Concerns*, pp. 257–279, 2013, doi: 10.1016/B978-0-444-53870-3.00010-1.

[4] N. Wakao, S. Kaguei, *Heat and Mass Transfer in Packed Beds, Gordon and Breach Science Publisher, New York, 1982*. Gordon & Breach, London, 1982.

[5] P. J. Handley, D., Heggs, “the Effect Packing of Thermal Conductivity Bed of the Material on Transient in a Fixed,” *Int. J. Heat Mass Transf.*, vol. 12, pp. 549–570, 1969.

[6] M. F. Edwards and J. F. Richardson, “Gas dispersion in packed beds,” *Chem. Eng. Sci.*, vol. 23, pp. 109–123, 1968, doi: 10.1016/0009-2509(68)87056-3.

[7] R. T. Driessen, S. R. A. Kersten, and D. W. F. Brilman, “A Thiele Modulus Approach for Nonequilibrium Adsorption Processes and Its Application to CO2 Capture,” *Ind. Eng. Chem. Res.*, vol. 59, pp. 6874–6885, 2020, doi: 10.1021/acs.iecr.9b05503.

[8] J. M. smith Ch. wang, “Tortuosity Factors for Diffusion in catalyst pellets,” vol. 29, pp. 132–136, 1983, doi: https://doi.org/10.1002/aic.690290118.

[9] J.W.Beeckman, “Mathematical description of Heterogeneous Materials,” *Chem. Eng. Sci.*, vol. 45, pp. 2603–2610, 1990.

[10] A. Blanc, “Recherches sur les mobilités des ions dans les gaz,” *J. Phys. Théorique Appliquée*, vol. 7, pp. 825–839, 1908, doi: 10.1051/jphystap:019080070082501.

[11] E. N. Fuller, P. D. Schettler, and J. C. Giddings, “A new method for prediction of binary gas-phase diffusion coefficients,” *Ind. Eng. Chem.*, vol. 58, pp. 18–27, 1966, doi: 10.1021/ie50677a007.

[12] B. E. Poling, J. M. Prausnitz, and J. P. O’Connell, *The Properties of Gases and Liquids*. McGraw-Hill Education, 2000.

[13] H. Ma, R. K. Sharma, S. Welzel, M. C. M. van de Sanden, M. N. Tsampas, and W. F. Schneider, “Observation and rationalization of nitrogen oxidation enabled only by coupled plasma and catalyst,” *Nat. Commun.*, vol. 13, pp. 1–22, 2022, doi: 10.1038/s41467-021-27912-2.

[14] P. Fang, J. Wang, X. Li, S. Wu, W. Zhang, and S. Li, “Effect of platinum on sintering morphology of porous YSZ ceramics,” *Microsc. Res. Tech.*, vol. 80, pp. 889–897, 2017, doi: 10.1002/jemt.22878.

[15] S. Yagi, D. Kunii, and N. Wakao, “Studies on axial effective thermal conductivities in packed beds,” *AIChE J.*, vol. 6, pp. 543–546, 1960, doi: 10.1002/aic.690060407.

[16] H. S. Fogler, *Elements of chemical reaction engineering*, 5th ed. Philadelphia, PA: Prentice Hall, 2016.

[17] E. W. Thiele, “Relation between Catalytic Activity and Size of Particle,” *Ind. Eng. Chem.*, vol. 31, pp. 916–920, 1939, doi: 10.1021/ie50355a027.

[18] A. Rutherford, *Introduction to the analysis of chemical reactors*. Englewood Cliffs, N.J., Prentice-Hall, 1965.

[19] T. B. J.K. Norskov, F. studt, F. Abild-pedersen, *Fundamental Concepts in Heterogeneous Catalysis*. Wiley & Sons, 2014.

[20] M. W. Chase Jr., *NIST-JANF Thermochemical Tables*. New York: National Institute of Standards and Technology, 1998.

[21] J. K. Nørskov *et al.*, "Universality in heterogeneous catalysis," *J. Catal.*, vol. 209, pp. 275–278, 2002, doi: 10.1006/jcat.2002.3615.

[22] H. Ma and W. F. Schneider, "Structure- and Temperature-Dependence of Pt-Catalyzed Ammonia Oxidation Rates and Selectivities," *ACS Catal.*, vol. 9, pp. 2407–2414, 2019, doi: 10.1021/acscatal.8b04251.

[23] A. Bajpai, P. Mehta, K. Frey, A. M. Lehmer, and W. F. Schneider, "Benchmark First-Principles Calculations of Adsorbate Free Energies," *ACS Catal.*, vol. 8, pp. 1945–1954, 2018, doi: 10.1021/acscatal.7b03438.

[24] C. E. Treanor, J. W. Rich, and R. G. Rehm, "Vibrational relaxation of anharmonic oscillators with exchange-dominated collisions," *J. Chem. Phys.*, vol. 48, pp. 1807–1813, 1968, doi: 10.1063/1.1668914.

[25] A. Fridman, *Plasma Chemistry*. Cambridge University Press, 2008.

[26] A. Ricard, J. P. Sarrette, S. G. Oh, and Y. K. Kim, "Comparison of the Active Species in the RF and Microwave Flowing Discharges of N2 and Ar–20 %N2," *Plasma Chem. Plasma Process.*, vol. 36, pp. 1559–1570, 2016, doi: 10.1007/s11090-016-9739-9.

[27] K. K. Irikura, "Experimental vibrational zero-point energies: Diatomic molecules," *J. Phys. Chem. Ref. Data*, vol. 36, pp. 389–397, 2007, doi: 10.1063/1.2436891.

[28] P. Mehta, P. Barboun, F. A. Herrera, J. Kim, P. Rumbach, D. B. Go, J., C. Hicks, W. F. Schneider, "Overcoming ammonia synthesis scaling relations with plasma-enabled catalysis," *Nat. Catal.*, vol. 1, pp. 269–275, 2018, doi: 10.1038/s41929-018-0045-1.

[29] S. De Benedictis and G. Dilecce, "Time resolved diagnostics for kinetic studies in N2/O2 pulsed rf discharges," *J. Phys. III*, vol. 6, pp. 1189–1204, 1996, doi: 10.1051/jp3:1996178.

[30] A. Ricard, J. P. Sarrette, B. Jeon, and Y. K. Kim, "Discharge source-dependent variation in the densities of active species in the flowing afterglows of N2 RF and UHF plasmas," *Curr. Appl. Phys.*, vol. 17, pp. 945–950, 2017, doi: 10.1016/j.cap.2017.04.006.

[31] E. Kemaneci, J. P. Booth, P. Chabert, J. Van Dijk, T. Mussenbrock, and R. P. Brinkmann, "A computational analysis of the vibrational levels of molecular oxygen in low-pressure stationary and transient radio-frequency oxygen plasma," *Plasma Sources Sci. Technol.*, vol. 25, p. 25025, 2016, doi: 10.1088/0963-0252/25/2/025025.

[32] P. Vašina, V. Kudrle, A. Tálský, P. Botoš, M. Mrázková, and M. Meško, "Simultaneous measurement of N and O densities in plasma afterglow by means of NO titration," *Plasma Sources Sci. Technol.*, vol. 13, pp. 668–674, 2004, doi: 10.1088/0963-0252/13/4/016.